Il Quaternario
Italian Journal of Quaternary Sciences
***22**(1), 2009 - 39-52*

SUBSURFACE VISUALIZATION USING GROUND-PENETRATING RADAR FOR ARCHAEOLOGICAL SITE PREPARATION ON THE NORTHERN SLOPE OF SOMMA-VESUVIUS: A ROMAN SITE, POLLENA TROCCHIA, ITALY

J. H. McBride†[1], R. W. Keach[1], R. T. Macfarlane[2], G. F. De Simone[3], C. Scarpati[4], D. J. Johnson[5], J. R. Yaede[1], G. S. Macfarlane[6], R. W. R. Weight[1]

[1]Department of Geological Sciences, Brigham Young University, Provo, Utah USA, e-mail: john_mcbride@byu.edu
[2]Apolline Project, Department of Classics, Brigham Young University, Provo, Utah USA
[3]St. John's College, University of Oxford, Oxford, United Kingdom
[4]Dipartimento di Scienze della Terra, Università degli Studi Federico II, Napoli, Italy
[5]Department of Anthropology, Brigham Young University, Provo, Utah USA

ABSTRACT: J. H. McBride *et al*., *Subsurface Visualization Using Ground-Penetrating Radar for Archaeological Site Preparation on the Northern Slope of Somma-Vesuvius: A Roman Site, Pollena Trocchia, Italy*. (IT ISSN 0349-3356, 2009).
The use of non-invasive geophysical techniques is becoming increasingly important in archaeological site studies as a means to increase the efficiency of excavation and to thereby avoid unnecessary disturbance. Ground-penetrating radar (GPR) surveys were performed over an orthogonal grid in order to guide the decision-making process for planning excavation at a Roman site in Pollena Trocchia (Italy), located just off the NW flank of Somma-Vesuvius. Archaeological planning for this site is complicated by contextual disruption and intermittent backfill, sometimes exacerbated by its proximity to building sites and by its use as a landfill, and by prior archaeological excavation and subsequent remediation. From a geophysical point of view, the site at Pollena Trocchia provided an ideal test-bed for visualization experiments (a) because the ground surface was readily cleared and smoothed by earth-moving machinery and (b) because the soil derived from geologically recent volcanic ash was dry at the time of the survey. State-of-the-art geophysical visualization techniques were applied to the pseudo-3D GPR data using conventional displays, seismic attribute analysis, and waveform connectivity schemes as employed in petroleum exploration. In this way, we assess the value of applying strategies adapted from industrial 3D seismic imaging to the problem of defining the effects of previous disturbance at a complex archaeological site.

RIASSUNTO: J. H. McBride et al*.,* Visualizzazione Subsuperficiale tramite Ground-Penetrating Radar per la Preparazione di un Sito Archeologico sul Versante Settentrionale del Somma-Vesuvio: un Sito Romano, Pollena Trocchia, Italia*. (IT ISSN 0349-3356, 2009)..*
L'uso di indagini geofisiche di tipo non-invasivo sta diventando sempre più rilevante nella ricerca archeologica, poiché incrementa l'efficienza dello scavo e riduce le attività non necessarie. L'indagine georadar (GPR) su griglia ortogonale è stata utilizzata per il sito romano nel comune di Pollena Trocchia (in provincia di Napoli, sul versante settentrionale del Somma-Vesuvio) per la pianificazione delle attività di scavo. L'area oggetto d'indagine risulta di complessa lettura, poiché disturbata da alcuni tagli e riempimenti relativi alla costruzione di edifici nelle vicinanze, alla scoperta del sito, ed al successivo accumulo di materiali. Dal punto di vista geofisico, il sito di Pollena Trocchia può essere considerato un caso-studio ideale per esperimenti di visualizzazione, in quanto: (a) la superficie risultava molto piana e ripulita dalla vegetazione spontanea con mezzo meccanico; (b) il suolo, di origine vulcanica, era particolarmente asciutto durante l'indagine. Le più recenti tecniche di visualizzazione geofisiche sono state applicate a dati pseudo-3D grazie all'uso di visualizzazioni convenzionali, analisi degli attributi sismici, e schemi delle onde di connettività simili a quelle utilizzate per le indagini petrolifere. In tale modo, è stato possibile valutare l'applicabilità di visualizzazioni sismiche 3D di tipo industriale per l'analisi di anomalie all'interno di un contesto archeologico

Keywords: radar, geophysics, Roman age, Italy, Vesuvius, volcanic.

Parole chiave: georadar, geofisica, età Romana, Italia, Vesuvio, riempimento vulcanico.

INTRODUCTION

The past several years have witnessed a steady expansion in using ground-penetrating radar (GPR) to provide images of the remains of human habitation and related building structures at buried archaeological sites (Conyers, 2004; Conyers, 2007; Goodman *et al*., 2007). With the ready availability of advanced, but easy-to-deploy field acquisition systems, GPR data can be surveyed along parallel lines or grids and processed into a pseudo-3D data volume (for the bistatic case with two bow-tie dipoles separated with a constant offset). Much of the published research on 3D GPR visualization has utilized computer applications that have been developed specifically for radar applications. In this study, we present the results of experimenting with state-of-the-art 3D visualization techniques and strategies adapted from petroleum exploration but applied to imaging the effects of previous episodes of excavation and ground disturbance at an archaeological site.

The study area is a locale known formally as Masseria De Carolis, a tract of vacant land in the town of Pollena Trocchia. Beneath the surface of the landscape a Roman site lies buried by volcanic deposits from Somma-Vesuvius. The site was found in 1988 (Pagano, 1992) during building excavations for the high-rise apartment complex nearby. Renewed interest since 2005 has made the site the focus of an ongoing archaeological study undertaken by the Università degli Studi "Suor Orsola Benincasa" of Naples and Brigham

Young University, with participating colleagues joining from other institutions. This team, called the Apolline Project, also includes the administration of the Comune di Pollena Trocchia. Most recent excavations were carried out by the Apolline team in Summer, 2007 (De Simone *et al*., 2007). This archaeological project seeks to add further knowledge to that ascertained by the preliminary excavations at the site by Pagano (1992).

Accurate detection and mapping of previous disturbance of the ground, it was reasoned, would be useful for planning future excavations and for avoiding confusion when interpreting the results of an excavation that may have crossed into an area previously disturbed. In this study we focus mainly on features that represent previous disturbance and not on possible archaeological features. The archaeological aspects of the site are only briefly mentioned here, in order to provide a setting for the GPR visualization analysis.

CULTURAL SETTING OF THE SITE

Discovery and project overview

The site at Masseria De Carolis was discovered accidentally in 1988 and studied in 1991-92. In an admittedly "brief excavation campaign," without achieving the floor of any space nor fully determining the plan of any complete room nor discovering any dating material, Pagano surmised that the site was a granary ("grandi magazzini di ammasso di prodotti agricoli") constructed in the 2nd century AD. Pagano posited, further, that disruption in the parietal fabric might have been caused by mid-18th-century quarrying at the site; perhaps it was the source of 12,000 bricks reportedly extracted from the area of Pollena and reused by the Bourbon kings in the building of the Teatro San Carlo in Naples. While Pagano's interpretation of the site seems more uncertain, as the Apolline Project goes forward, his optimism that the site will yet reveal important evidence for the ancient economy on Vesuvius' northern slope seems certain to be confirmed.

Pagano (1992) refers to a trench measuring 10 x 10 m, which he sunk with earth-moving equipment "a short distance north-east" of the Roman walls that comprise the site itself. While his publication does not specify the location of that trench, the negative conclusions he records are important for certifying that the ancient building's lateral profile did not extend far from the walls he discovered. The location of that trench will be discussed in this article, below.

After the brief archaeological campaign reported by Pagano, the Masseria De Carolis was returned nearly to *its status quo ante*. A wire fence was strung around wooden posts to demarcate the central area of the 1990's excavation; all other areas in the lot were backfilled with construction rubbish. Illegal disposal of more-or-less clean fill occurred over time, and by 2006 even the fenced section had been compromised and filled with trash. Nearly all signs of earlier excavation were again buried beneath the landscape's surface.

Description of archaeological features

Field work activities during the 2007 archaeological campaign brought new relevant data for understanding not only the site itself, but also the broader geographical and cultural frameworks, almost unknown until recently (De Simone, 2007). The excavation, the analysis of material cultural remains, and - more broadly - the multidisciplinary project itself are still in a preliminary phase; thus it is impossible to define clearly the character of the site and the phases of its occupation. Nevertheless, the description of what is currently visible is fundamental (a) for understanding the reasons for the setting of the GPR test areas and (b) as a comparative data set for what we would (or would not) expect to find in the GPR test areas.

The area appears essentially flat and almost at the same level of the archaeological remains, due to the excavations performed in the '80s. On the east side, where one of the GPR test areas is, the ground rises for about 1.5 m above the archaeological remains. South of the site, in the area used in the '80s as quarry for volcanic ash, the trash illegally dumped there is still present and makes it therefore difficult to define the boundaries of the ancient structures in that area.

The visible archaeological remains show at least 7 rooms, most of which are still partially or completely roofed (Fig. 1b: A, B, C, D). There are still traces in some points (C, E, F) of the ancient *cocciopesto* pavement. This information, together with the collapse remains of some walls (G, H), lead us to the conclusion that the structure had an upper floor. The structures now visible are probably built in the 2nd/3rd century AD on the top of a pre-79 AD building, as the presence of fresco fragments and volcanic ash beneath the foundation trenches suggests. The building was used for a few centuries, then buried as much as two thirds of its height by the late-antique 472 AD eruption. The dating of volcaniclastic materials is confirmed by the presence, in the last anthropized context, of a burial of a six-year-old boy with a bronze coin dated to the period of Marcian (Emperor of the Eastern Roman Empire in 450-7). On the top of the 472 volcanic fill are bricks and stones taken from the surrounding walls packed together for raising the floor level. On the top of it is a poorly-made oven (I), sealed together with the surviving remains of the building by the 512 AD and subsequent eruptions (see following paragraph).

GPR analysis was set up for hypothesizing, in a non-destructive and time-efficient manner, how and in which direction the building continues underground. The choice of the areas for performing the GPR scanning was determined by several considerations on the surviving structures: the remains of *cocciopesto* floor on the east side of the site (F) suggest in fact the continuation of the structures beneath the latest fills, with the presence of a probably well preserved room beneath it. The other side of the building seemed a quite promising area as well, for all the rooms are aligned along an E-W axis and therefore we expected more structures along that axis. Moreover, the *cocciopesto* floor E shows no clear boundaries on the north side, therefore the NW corner was the most promising area for performing large-scale GPR analysis. The south side of the site, as explained above, was used in the '80s as quarry for construction materials and then filled by illegal dumping. Consequently no GPR could be performed along this side of the structure.

PHYSICAL GEOLOGY OF THE SITE

General Background

The Pollena Trocchia archaeological site is located on the northern slope of Somma-Vesuvius at an elevation of about 90 m. The site covers an area of almost 400 m^2 and has been excavated to 5 m as of Summer 2007 (Fig. 1). The excavation has revealed a large Roman building, which had been buried by pyroclastic and reworked volcaniclastic deposits belonging to the Somma-Vesuvius volcanic complex. Because the GPR surveys were targeting features within the volcanic products, we summarize the stratigraphy of the volcanic succession. The Somma-Vesuvius volcanic complex results from repeated explosive eruptions, usually from a central vent, that produced stratified pyroclastic deposits and lava flows (SANTACROCE, 1987; SULPIZIO *et al*., 2007). The volcanic products erupted by Somma-Vesuvius are not ubiquitously distributed around the volcano but crop out according to their eruptive and emplacement mechanisms and the topography.

Toward the summit of Somma-Vesuvius and along the axis of the most deeply excavated valleys, ancient lavas and scoria cones are exposed. The products of this prevailing effusive activity are covered by the products of explosive eruptions ranging from weak strombolian (e.g., 1874 eruption) to extremely powerful plinian (e.g., 79 AD eruption). The products of numerous pyroclastic density currents are well exposed along the volcano's northern flank. Thick and massive deposits are confined in the valleys that flowed from the volcano; conversely, thinly stratified deposits crop out on the interfluves and in the plain. Heavy rainfall occurring during and after the explosive eruptions generated floods that easily eroded and mixed largely uncompacted primary deposits to form lahars. Lahars, which are generated on the steep slopes above, inundated areas far away from their sources. The resulting deposits occur in the valleys and on lowlands (PERROTTA *et al*., 2006a; b), including Pollena Trocchia.

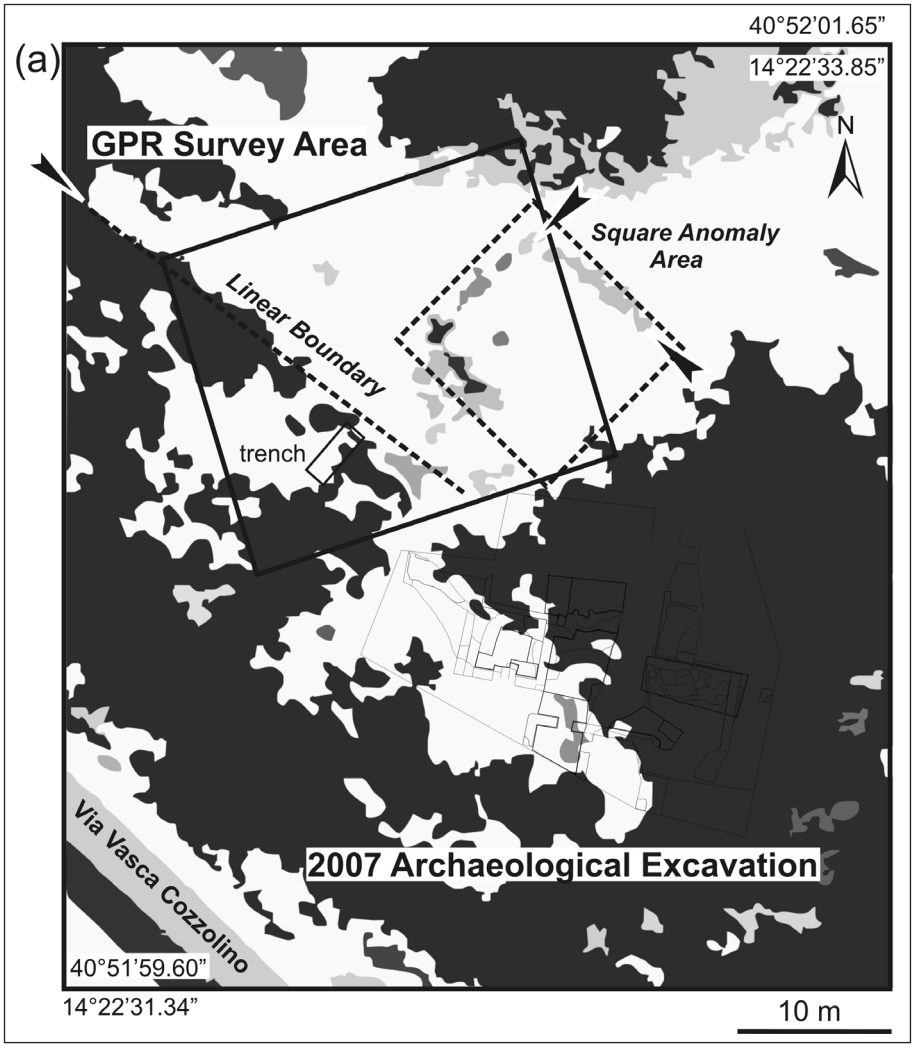

Figure 1 - (a) Location map for GPR survey and archaeological excavation underway as of Summer 2007 (DE SIMONE *et al.*, 2007). The map is rendered as patterns observed from an aerial photograph of the site on which higher intensity mostly represents vegetation and lower intensity mostly represents bare or poorly vegetated ground. [Map overlay: Massimo Manfellotto] (b) Schematic map of the archaeological site and GPR survey areas. [Drawing: Salvatore Borrelli; Editing: Massimo Manfellotto].

(a) Localizzazione dell'indagine GPR e dello scavo archeologico in corso nell'estate 2007 (DE SIMONE et al.*, 2007). La pianta è realizzata con tematizzazioni tratte dalla foto aerea del sito: il tratteggio più denso rappresenta la vegetazione, quello meno denso le aree povere o prive di vegetazione. [Mappa sovrapposta: Massimo Manfellotto] (b) Mappa schematica del sito archeologico e dell'area indagata con GPR. [Disegno: Salvatore Borrelli; Edizione: Massimo Manfellotto].*

Volcanic Stratigraphy

The exposed sequence in the excavation site is made up of seven stratigraphic units (Fig. 2). Each unit is denoted by a letter from A to G younging upwards. The basal volcaniclastic sequence consists of five, decimeter to about 2 m thick, massive deposits (A1, A3, A5, A7 and A9) interstratified with thin ashy horizons (A2, A4, A6 and A8) (Fig. 2). Massive deposits are matrix-supported and lithic-rich. The matrix is light brown in color. Lithic clasts are up to 12 cm in diameter and generally not graded. Lithic types include reddish altered lavas, gray aphiric lavas and limestone fragments that range in shape from angular to rounded. Thin ashy layers are stratified and show a lateral variation in thickness. Scattered whitish pumice clasts are dispersed in these layers.

A thin paleosol separates this volcaniclastic sequence

from a thinly stratified deposit (B1), defined by the alternation of fine-grained, plane-parallel laminae interlayered with coarse ash layers (Fig. 2). The upper bed, B2, is comprised of thick, stratified ash layers. A thin reddish paleosol is observed at the top of the succession. Unit B is overlain by a stratified deposit (C1 to C3). This horizon is covered by a thick paleosol (P4). The remnant part of the succession is made up by four thin pyroclastic layers (D, E, F and G) interstratified with paleosols. Layer D is a laterally discontinuous, fine ash layer. Layer E is a massive, well sorted, fine lapilli gray scoria layer. The coarse-ash layer F is discontinuous, with abundant lithic fragments. Finally, the fine ash layer G shows rare scoria dispersed in the matrix.

The stratigraphic units are tentatively correlated with the historical eruptions of Vesuvius on the basis of their lithostratigraphic characteristics. Above the Roman floor as currently excavated, the products consist of thick volcaniclastic beds (Unit A) (Fig. 2) associated with the 472 AD Vesuvius eruption. As stated above this correlation is strongly supported by the presence of a coin dated 450-457 at the base of this deposit. The 472 AD deposit is capped by a very discontinuous and thin paleosol that is covered by stratified and massive ash-bearing beds (unit B). The presence of a poorly developed soil suggests that the products of unit B were emplaced after a brief quiet period following the 472 AD eruption and are consequently related to the 512 AD eruption. The upper, thin pyroclastic deposits are possibly related to the medieval eruptions of Vesuvius; in particular layer F could be associated to the 1631 eruption. As part of this study, we excavated a small trench in the SW corner of the survey area (Fig. 3). The results of the trench locally show two layers: (1) an upper layer, between the surface and 0.5 m depth, of modern soil and modern soil mixed with building rubbish (e.g., tiles, rebar, electrical wiring, etc.); and (2) a deeper layer of stratified volcanic ash.

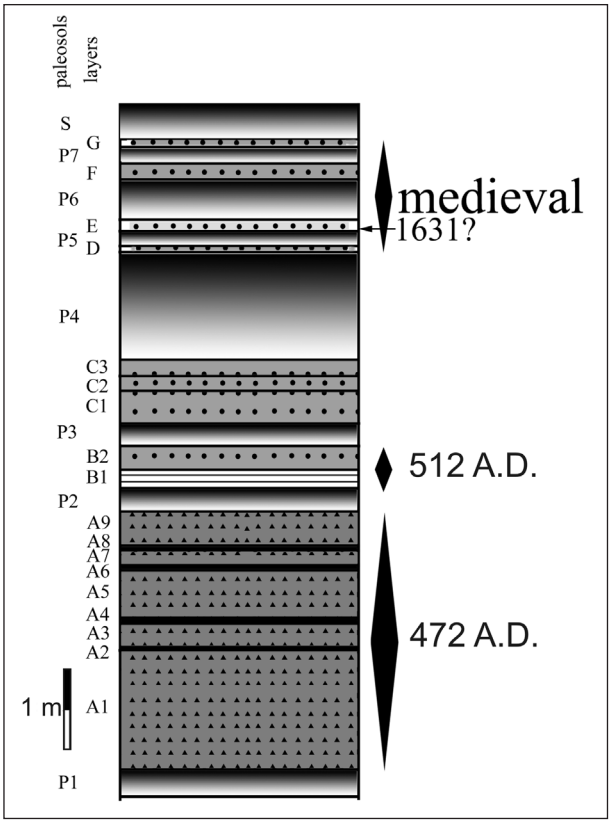

Figure 2 - Stratigraphic column for the volcanic succession at the Pollena Trocchia site with interpreted intervals of eruptions noted. Triangles: lithic-rich 472 AD deposits; circles: ash and pumice post-472 AD deposits; gray darkening upwards: paleosol.

Colonna stratigrafica della successione vulcanica del sito di Pollena Trochia con annotazione interpretativa degli intervalli eruttivi. Triangoli: depositi dell'eruzione del 472 d.C. ricchi in litici; cerchi: ceneri e pomici delle eruzioni post-472 d.C.; campi in grigio che si scuriscono verso l'alto: paleosuoli.

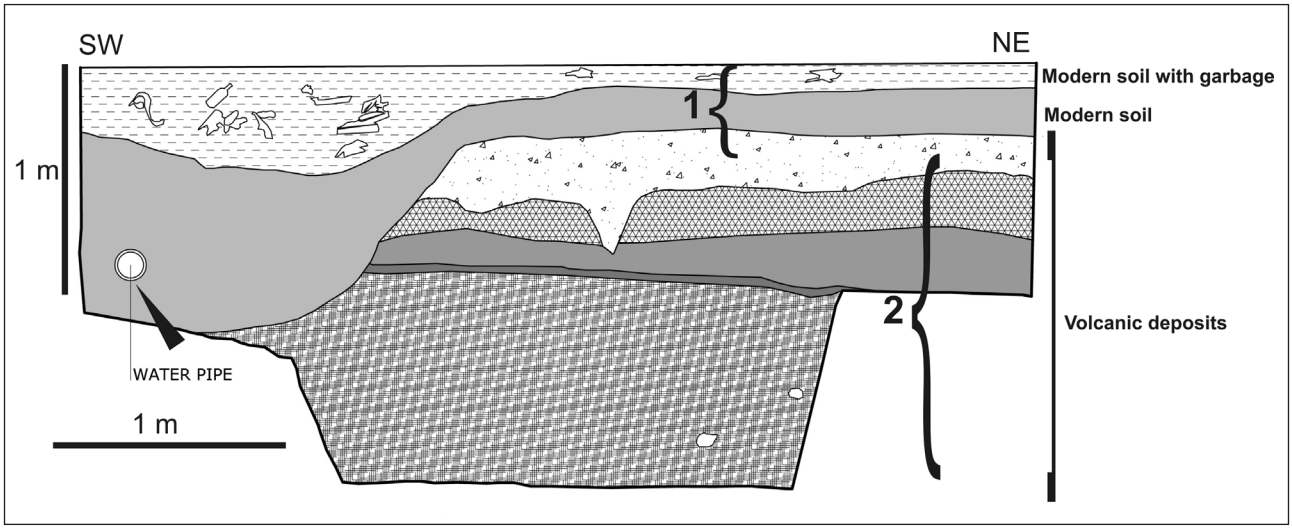

Figure 3 - Interpretation of soil and volcanic layering from the trench excavated near the SW corner of the GPR survey site (Fig. 1). "1" and "2" refer to layering observed in the GPR vertical views (Fig. 5). The patterns on the drawing represent differing materials observed in the trench. [Drawing: Annie Peterson; Digitization: Massimo Manfellotto].

Interpretazione della stratificazione vulcanica e del suolo nel saggio scavato nei pressi dell'angolo SO del sito indagato (Fig. 1). '1' e 2' si riferiscono alla stratificazione osservata nella sezione verticale del GPR (Fig. 5). I motivi nel disegno rappresentano i diversi materiali osservati nel saggio. (disegno: Annie Peterson; Digitalizzazione: Massimo Manfellotto).

GPR DATA

Data Acquisition

Dry volcanic ash, such as covers our study area, can provide an ideal medium because of its relatively low clay content, low electrical conductivity, and orderly stratification. GPR has been successful in revealing the pre-excavation configuration of archaeological sites buried by volcanic ash or volcaniclastic deposits in many places (e.g., RUSSELL & STASIUK, 2000). Perhaps the best known example, apart from the well-known Vesuvian sites such as Pompeii, is the Joya de Ceren archeological site in El Salvador (SHEETS, 2005). The rapid burial of the site under several meters of volcanic ash led to the remarkable preservation of the daily life activities, food, and personal belongings of this pre-Columbian community.

The radar survey at Pollena Trocchia used a GSSI 400-MHz antenna and recording unit in bistatic mode (transmitter and receiver set at a fixed distance within the antenna casing). An orthogonal grid was surveyed over a rectangular areas of ~520 m^2 (5600 ft^2) with lines spaced at ~0.30 m (1 ft). The survey areas were positioned so as to be as close as possible to the present excavation (DE SIMONE *et al*., 2007) (Fig. 1). Positioning of the GPR tracks was constrained by exact measurements on the ground and guided by a network of string. The GPR tracks were acquired in continuous mode at 512 samples per scan over a range of 70 ns, ~79 scans/m (24 scans/ft), and 64 scans/s. The field acquisition filter was set to a low-pass of 800 MHz and a high-pass of 100 MHz.

Data Processing

The processing of the GPR data was complicated by the presence of modern landfill material, the distribution of which was not known prior to the survey, and by the presence of previous archaeological excavations, which had been back-filled. The 2D processing was performed using RADAN™ software in which geometry assignment, surface correction, background (direct wave) removal, deconvolution, and constant-velocity migration were performed. The background removal was performed using a horizontal boxcar filter based on a 500-trace width. A predictive deconvolution using an operator length of 31 ns, and prediction lag of 5 ns, and a 10% pre-whitening noise addition was then applied. The purpose of this step was to help eliminate the effects of short-period multiple arrivals from interbed echoes and to compress the waveforms. In order to boost weak amplitudes deeper in the section that suffered loss due to spherical spreading or attenuation, a variable automatic gain control was designed using six points along the travel time record. A bandpass frequency filter was applied between 200 and 400 MHz so as to reduce the effect of noise admitted by the broader bandwidth field filter. This application was accompanied by a 9-trace mix ("running sum"), which was aimed at removing low-apparent velocity noise, especially apparent deeper on the records. Such noise typically arises in part from random scattering.

For this study, we observed a range of dielectric constants based solely on diffraction hyperbolae with typically high values of 9.17 and as low as 4 (Fig. 4). The range of velocities of the material overlying the diffraction apices probably reflects the complexity of material, manmade and geologic, at the site. A dielectric constant of 4 corresponds to a velocity of about 0.15 m/ns, while for a dielectric constant of 9.17, the velocity is 0.099 m/ns. Near the SW part of the survey, a buried section of PVC pipe was observed in a trench dug as part of this study (to be discussed below) (Fig. 3) at a depth of about 0.89 m, that corresponds to a linear GPR anomaly arriving at 21 ns, which yields a velocity of 0.085 m/ns and a dielectric constant of 12.5. The study of RUST *et al*. (1999) of the dielectric constant for dry volcanic rocks gives values as low as about 2 and as high as about 18. RUSSELL & STASIUK (1997) measured a dielectric constant of 9 for a Holocene pyroclastic flow in Canada. In order to remove the effect of diffractions and correctly position dipping events, we applied a Kirchhoff migration with a velocity (0.1 m/ns) corresponding to a dielectric constant of 9, which is within the middle of the range, and broadly consistent with the diffraction modeling, expectations for volcanic ash, and the dry conditions observed at the site. The travel times for the vertical views and the time slices can be converted to depth for a particular velocity assumption. For example, for a dielectric of 12.5, divide the travel time by 2 and multiple by 0.085 to obtain depth in meters.

GPR DATA VISUALIZATION

Following the 2D processing, the profiles were arranged into a grid and the amplitudes interpolated between lines to produce a pseudo-3D volume which could be viewed simultaneously as depth slices (maps) and vertical views (cross sections) using conventional 3D viewers as typically supplied by GPR software vendors. In order to provide an alternative viewing strategy, the profiles were next converted into SEG-Y format and imported into a suite of petroleum exploration industry visualization and post-stack processing software (SeisWorks3D™ and GeoProbe™, Halliburton). The profiles 82-152 were imported as "lines" and the individual traces within each profile constituted "traces" 1-1917, using the usual terminology for 3D seismic data processing. In this way, we were able to take advantage of a suite of seismic attribute and other volume processing strategies, usually reserved for exploring for underground petroleum reservoirs. We employed both map-based volume visualization and volume rendering techniques (MA & ROKNE, 2004). The former involves generation of traveltime-slices and surfaces mapped from subsurface reflectors and the latter dividing the volume into 3D data elements ("voxels") that can be assigned a value from a particular mathematical process (e.g., semblance) performed across the entire data volume. Volume rendering techniques take advantage of applying varying levels of transparency to the data and thus allow viewing more than one attribute of the data simultaneously. For more background on 3D volume visualization the reader is referred to MA & ROKNE (2004).

Conventional Views

A conventional vertical view cutting across the upper, NW part of the survey area shows a stratigraphi-

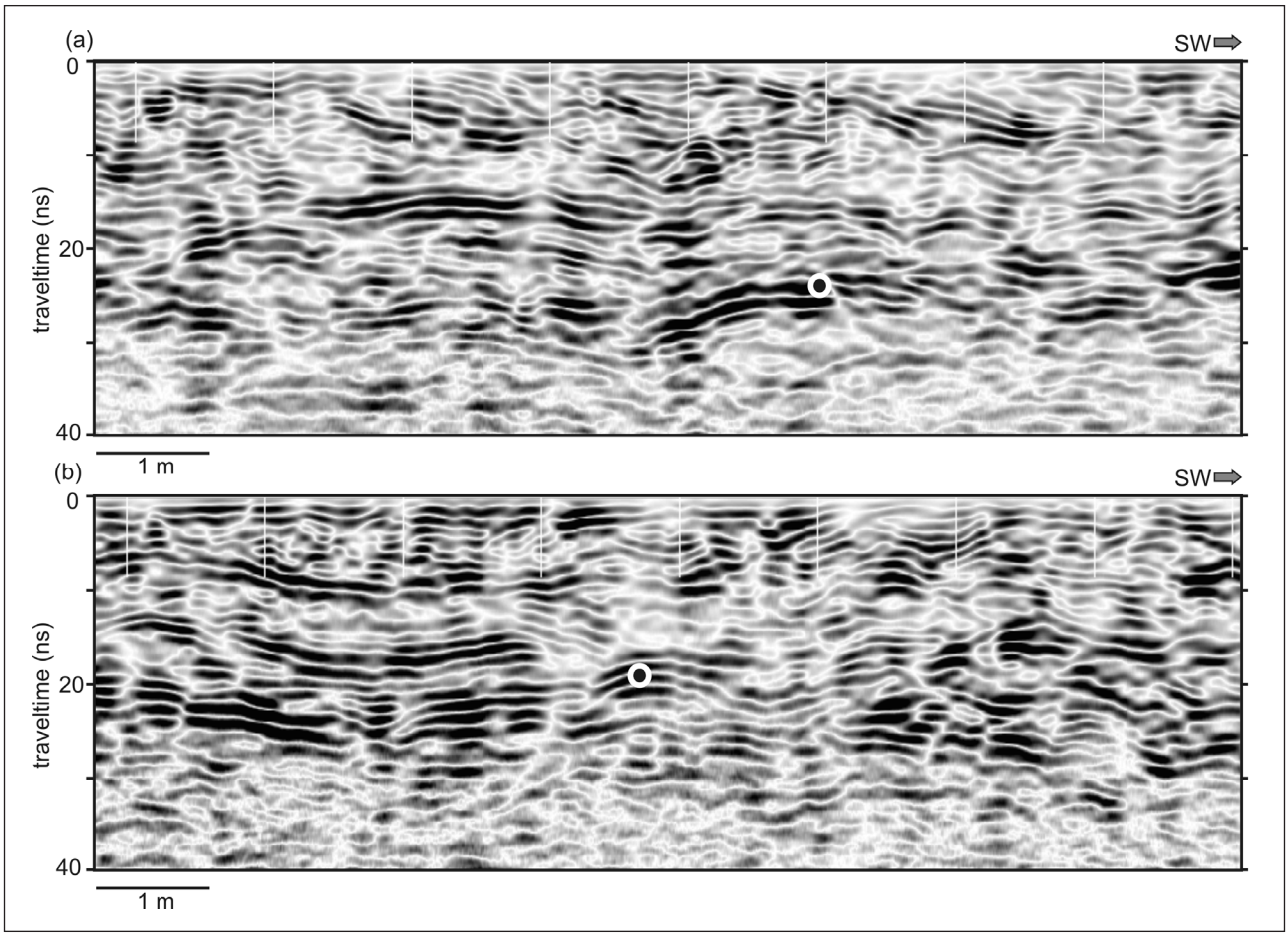

Figure 4 - Two vertical views (profiles) excerpted from the GPR data set (unmigrated) showing examples of diffractions (circles) used for estimating bulk velocity of the medium above the diffractor. (a) The diffraction collapses optimally for a migration velocity of about 0.15 m/ns, corresponding to a dielectric constant of 4. (b) The diffraction collapses optimally for a migration velocity of about 0.099 m/ns, corresponding to a dielectric constant of 9.17.

Due sezioni verticali (profili), estratte dai dati GPR (non migrati), mostrano esempi di diffrazioni (circoli) usati per stimare la velocità del mezzo a tetto del diffrattore. (a) La diffrazione è corretta in modo ottimale per una velocità di migrazione di circa 0,15 m/ns, che corrisponde ad una costante dielettrica di 4. (b) La diffrazione è corretta in modo ottimale per una velocità di migrazione di circa 0,099 m/ns, che corrisponde ad una costante dielettrica di 9,17.

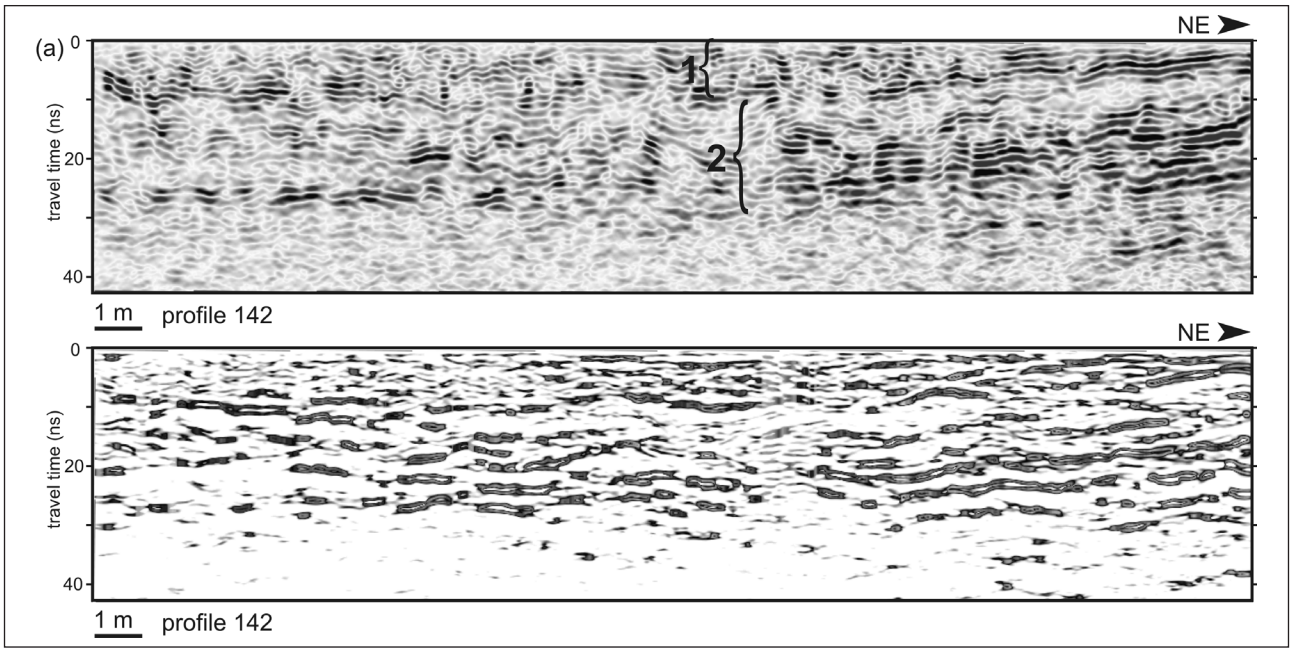

cally well-layered reflective sequence underlain by a boundary reflection that arrives at about 37 ns on the SW end of the profile (142, Fig. 5a) and rises up to 23 ns on the NE end. A second such profile across the approximate center of the survey area (113, Fig. 5b) shows the same reflective sequence over most of the SW part of the profile, but with abrupt lateral cessations of reflections and intervening zones of poor or chaotic reflectivity. Lastly, a profile through the SE part of the survey area (82, Fig. 5c) depicts a return to a well-stratified reflective sequence beginning on the NE end until about three quarters along the profile where again an abrupt lateral truncation of reflectivity appears. In general, two sequences of reflectivity are observed, an upper sequence from about 1 ns to 9 ns, followed by a deeper and thicker sequence from 10 ns to 31 ns (Fig. 5). We have created a conventional time slice view centered at 20 ns travel time with a vertical width of ~11 ns

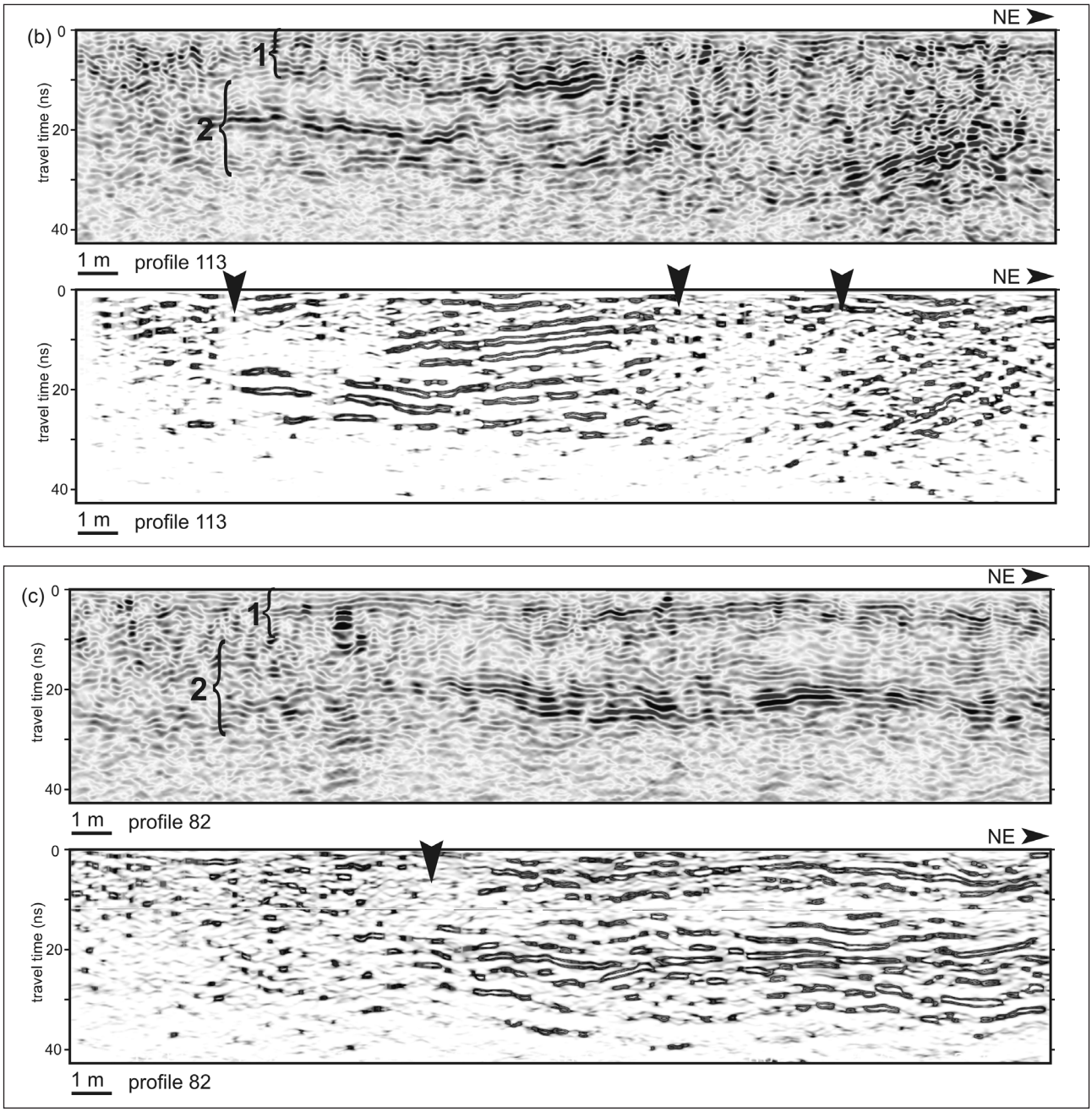

Figure 5 - (a) Top, conventional vertical view for profile 142 (see Fig. 6 for location). Lighter gray represents positive amplitudes, darker gray negative. "1" and "2" refer to layering observed in the GPR vertical views (Fig. 5). Bottom, vertical view extracted from the discontinuity attribute volume along the same line of profile. (b) Same as above, but for profile 113. (c) Same as above, but for profile 82. Vertical arrows indicate locations of abrupt lateral reflectivity terminations.

a) In alto, profilo verticale convenzionale del profilo 142 (vedi Fig. 6 per la localizzazione). Il grigio chiaro rappresenta ampiezze positive, il grigio scuro negative. '1' e '2' si riferiscono alla stratificazione osservata nelle sezioni verticali del GPR (Fig. 5). In basso, sezione verticale estratta dalla discontinuità del volume attribuito lungo la stessa linea di profilo. (b) Come sopra, ma per il profilo 113. (c) Come sopra, ma per il profilo 82. Le frecce verticali indicano il luogo della brusca terminazione di riflettività laterale.

(or ~1 m and width of ~0.5 m for a dielectric constant of ~9.2) over which all the amplitudes are displayed with a median filter for horizontal smoothing (Fig. 6). The broad width of the display zone shows the normalized (by the average amplitude) maximum amplitude for all samples in the "slice". The broad width was necessary to detect the subtle boundaries and edges as noted by arrows (Fig. 6), although this significantly decreases the depth resolution of the image since the display is combining information from a range of depths.

If we compare the three vertical views (Fig. 5) with the conventional travel time slice (Fig. 6), we can see that the disruptions on the vertical views correspond to boundaries between groups of positive and negative amplitude. Negative amplitude areas on the time slice (dark gray in Fig. 6) tend to correspond to low reflection coherency while positive amplitudes (light gray) usually correspond to higher coherency. Several linear and rectangular elements appear on the time slice. Here we discuss only the most obvious features, which are (1) the linear, NW-SE-trending boundary separating a reflective and an unreflective region to the NE and SW, respectively; and (2) an approximately square feature of low reflectivity near the eastern corner of the study area. These two features, together with the internal reflectivity of the stratigraphically layered sequence, are the focus of advanced seismic attribute and other visualization discussed next.

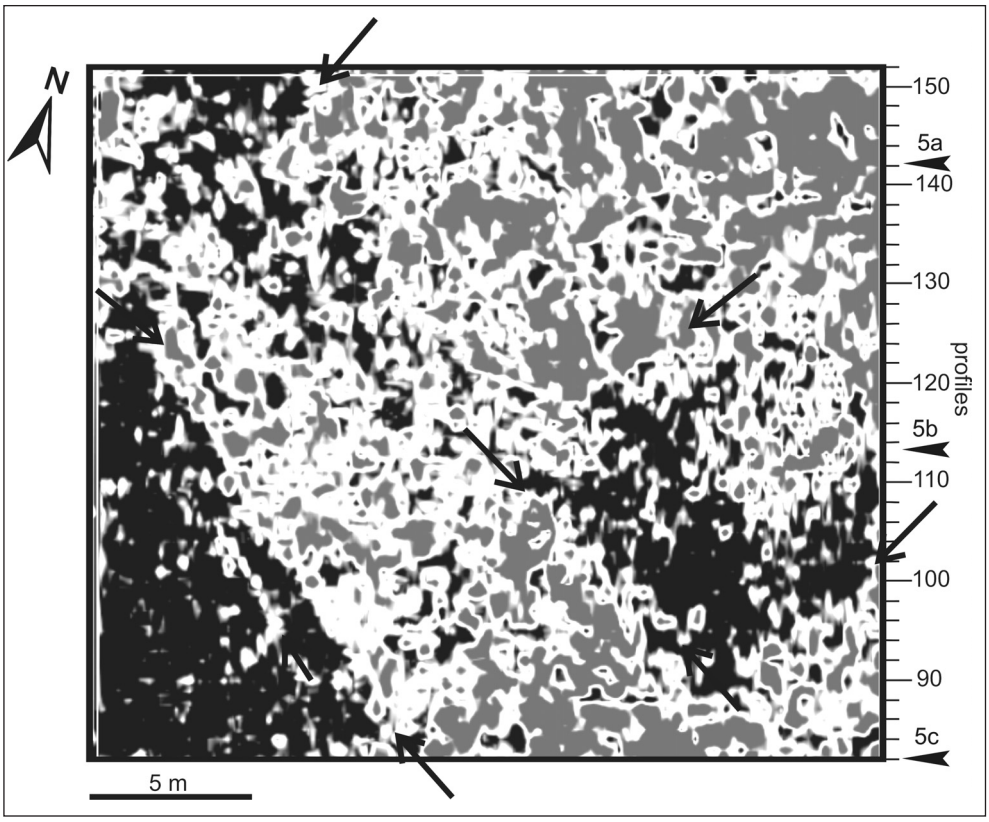

Figure 6 - Conventional time slice using a travel time interval of ~11 ns centered over 20 ns. Lighter gray represents positive amplitudes, darker gray negative. Arrows indicate boundaries or areas of interest, discussed in the text. Compare this and other map views with Fig. 1 for orientation and relation to surface features. The locations of the profiles shown in Figure 5 are indicated.

Mappa di tempo convenzionale prodotta usando un intervallo di tempo di percorrenza di circa 11ns centrati su 20 ns. Il grigio chiaro rappresenta le ampiezze positive, il grigio scuro le negative . Le frecce indicano i confini delle aree di interesse, discusse nel testo. Comparare questa e le altre mappe con la figura 1 per l'orientazione e la relazione con le caratteristiche superficiali. Sono indicate le localizzazioni dei profili mostrati in figura 5.

Advanced Views Based on Seismic Attribute and other Strategies

Discontinuity Attribute. Because the GPR features of interest in this study appear to be defined by terminations in reflectivity, we first applied a seismic discontinuity detection attribute to the data volume. Many different types of discontinuity attribute processes have been developed (e.g., BAHORICH & FARMER, 1995), but all basically seek to quantify the degree to which adjacent waveforms differ between traces. Abrupt lateral changes in waveform character that could be due to geological discontinuities (e.g., faults, stratigraphic terminations) are enhanced by this attribute. The technique applied here uses a weighted correlation to establish similarity between two traces based on a moving window that is parameterized according to the number of profile lines, number of traces, and a travel-time gate. For our study, we used a relatively wide spatial and time window (11, 11, 5 samples or ~0.7 ns), which enhanced profile views (Fig. 5, bottom sections), producing much cleaner images, but sacrificing some detail due to averaging in the window. The attribute is applied to the entire volume and then vertical views are extracted (Fig. 5, bottom sections) and shown along with the three conventional views (Fig. 5, top sections) as discussed above. The resulting profiles much more clearly show the positions of lateral reflector terminations as well as show regions of higher coherency, including the two general sequences of reflectivity referred to in the previous section. The terminations tend to affect the volume beginning at a fairly shallow level and continue deeper along a straight vertical line of discontinuity.

3D Volume Rendering. The 3D volume attribute computations used only one profile direction, NE-SW, and included 71 profiles (~0.3-m (1-ft) spacing), between which amplitudes were interpolated. The first visualization employed (Fig. 7) a volume rendering whereby all voxels inside a volume ranging from 18 ns to 24

ns are displayed simultaneously as if the space were semi-transparent (CASTANIE *et al.*, 2005). By rendering a volume semi-transparent it is possible to "see" anomalies from a range of travel times (depths) together in such a way that anomalies that remain consistent with depth are emphasized (or "stacked") and can be projected onto a map view (Fig. 7). In the volume rendering shown in Figure 7, only the highest positive amplitudes are mapped to black (or opaque within the volume; other amplitudes are mapped to zero or transparent), which emphasizes linear boundaries where amplitude abruptly decreases. However, this strategy mixes amplitudes in the display from a range of travel times, analogous to the conventional display in Figure 6, discussed in the previous section. The volume rendering displays several linear and rectilinear elements. Near the SW corner of the study area, three parallel NW-SE-trending linear elements can be recognized (Fig. 7). One of these linear anomalies corresponds to the buried pipe (Fig. 3), as discussed above, while the northeasternmost linear anomaly corresponds to a boundary between coherent and poorly coherent reflectivity (from NE to SW, respectively). Looking further to the NE, the outline of the approximate square can be easily seen (Fig. 7). The boundaries of the square are sharply delineated, suggesting that, since the 3D attribute represents a volume ranging from 18 ns to 24 ns, the sides of the square continue up and down as vertical edges surrounding a mostly incoherent region. This is also indicated by the enhanced vertical views that cut through the square (Fig. 5, bottom sections). The appearance of amplitudes (black color) within the square imply the presence of coherent features somewhere within the volume subset defined by the square in 2D.

3D Semblance Attribute. The semblance attribute (e.g., NEIDELL & TANER, 1971) computes a new 3D volume using the similarity of each trace with three neighboring traces with a travel time window length of 48 samples (about 6.6 ns). The relatively long window reduces noise, but may be smearing discontinuities. Like the discontinuity tool discussed above, semblance can highlight boundaries related to sudden changes in geological structure (or, in our case, shallow soils and sediments). The results of the computation (Fig. 8) indicate an area of low semblance (white in Fig. 8) within the square area and within the SW corner of the survey area. The semblance display is somewhat similar to the volume rendering except that the former represents one travel time (in this case, 8 or 18 ns, Figs. 8a and 8b, respectively), whereas the latter gathers information from 18 ns to 24 ns, and is thus less precise. The shallow time slice (Fig. 8a), which slices through the shallow reflective sequence, shows a comparable expression of low similarity within the square area compared to the previous attribute (cf. Figs. 8a and 7), although the edges of the square, especially on the western corner, are less distinct. However, the deeper slice (Fig. 8b) indicates a distinct linear element cutting across the SW corner of the survey area. This feature would not be as recognizable from the volume rendering alone (Fig. 7). On the other hand, the shallower slice (Fig. 8a) shows a narrow band of high coherency just around the NW corner of the square area that is not so apparent on the deeper slice (Fig. 8b). The semblance attribute is thus able to extract relatively minute details from the volume at just one time slice, whereas transparent volume renderings (Figs. 6 and 7) are averaging information over a range of travel time (i.e., depth).

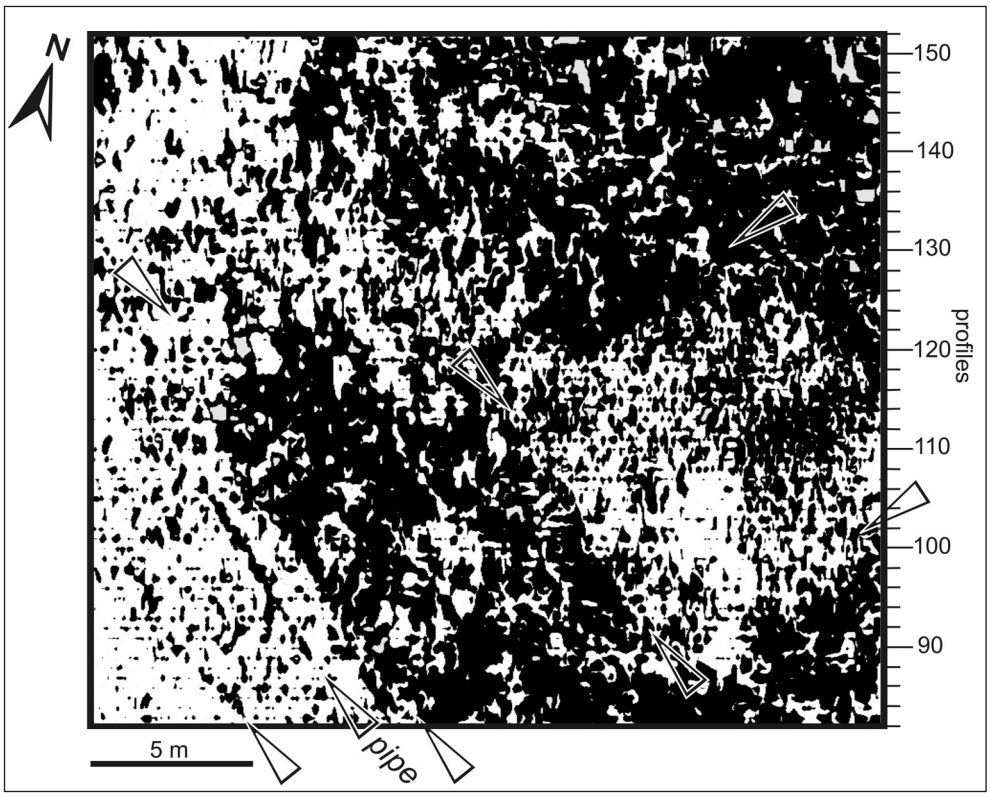

Figure 7 - Volume rendering of highest amplitudes for travel time interval of 18 ns to 24 ns. White represents negative amplitudes, black positive amplitudes. Faint horizontal striping is an artifact of the data acquisition.

Restituzione del volume per le ampiezze maggiori per tempi di percorrenza da 18 ns a 24 ns. Il bianco rappresenta ampiezze negative, il nero ampiezze positive. Le deboli strisce orizzontali sono un artefatto dell'acquisizione dati.

3D Arc Length Attribute. Arc length is a measure of the total excursion of the trace wiggle over a specified travel time window length (in this case, about 2 ns). Arc length can be described as a hybrid attribute that combines amplitude and frequency components and is proportional to amplitude, and higher values of arc length represent higher reflectivity (black in Fig. 9)

(SCHULTZ *et al*., 1994; RANA *et al*., 2006). Qualitatively, arc length is similar to reflection strength. Using the arc length attribute can increase the precision of the processed image because it depends on the phase of the waveform and thus may avoid the smearing of amplitudes due to interference and phase changes (RANA *et al*., 2006). The results for 12 ns (Fig. 9a) show a distinctive border of low arc length that defines the square area, which itself is composed of mixed high and low values. This mixed amplitude behavior can be compared with other areas of more consistently high (black) and low (white) arc length as seen, for example, in two north-south-trending bands of high and low arc length in the SW part of the survey area. At a time slice of 21 ns (Fig. 9b), the square anomaly is not well delineated; however, it is now possible with this attribute to isolate in depth the anomaly caused by a pipe as seen in the volume rendering (Fig. 7). As applied to this data set, the arc length processor is useful for detailed delineation of subtle boundaries.

Connectivity Attribute. An attribute has been developed based the 6-way connectivity between adjacent voxels in the volume. An anomaly will be identified and plotted when at least one face of the voxel is connected to a neighboring voxel (see ZHOU (1993) and GAO (2007) for examples). Connectivity has been used to produce a texture-based classification of a volume (GAO, 2007) that can then be used to delineate or map geological or soil features that

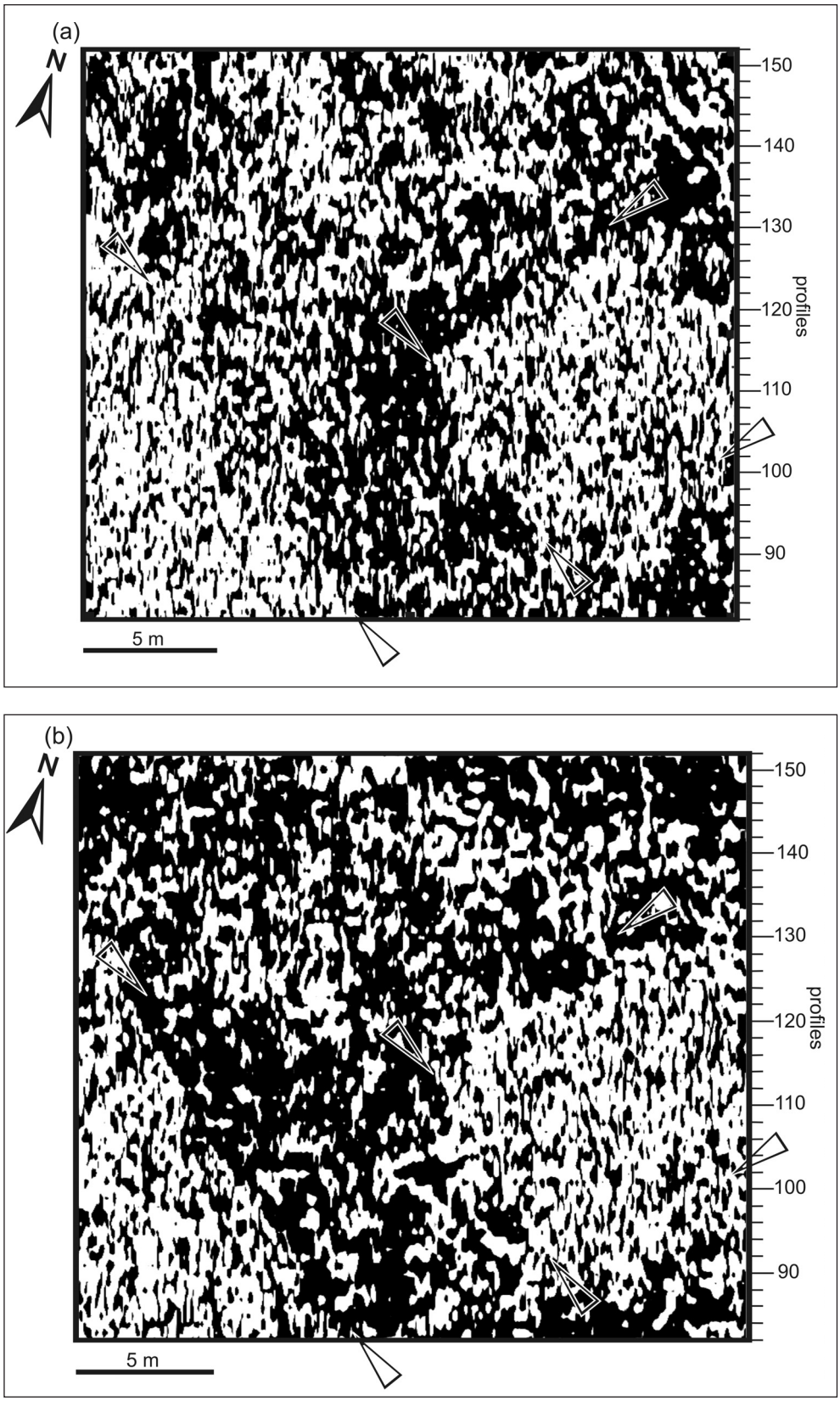

Figure 8 - (a) Map of semblance attribute for 8 ns, computed with a window length of 48 samples (about 6.6 ns), and a 3-trace sampling pattern. Low semblance is represented by white, high semblance by black. (b) Same as above, but for travel time of 18 ns.

(a) Mappa di 'semblance attribute' (vedi testo) per 8 ns, calcolata con una finestra di 48 campioni (circa 6,6 ns), e un campionamento a tre tracce. La basso valore di semblance è rappresentata dal bianco, l'alta dal nero. (b) Come sopra, ma per tempi di percorrenza di 18 ns.

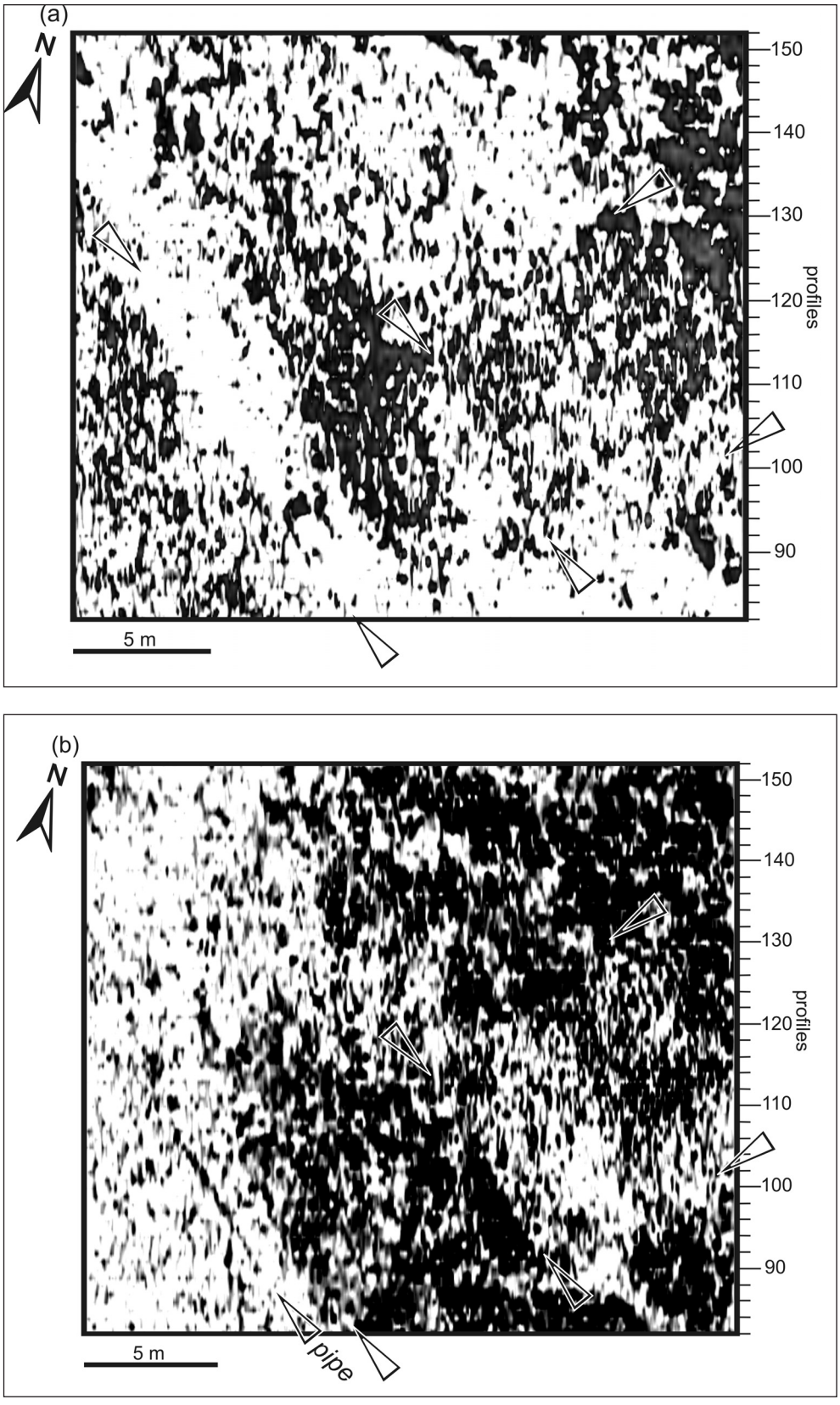

Figure 9 - (a) Arc length time slice, computed with a window length of 15 samples (about 2 ns) at 12 ns. Higher values of arc length are shown as black and are proportional to higher reflectivity. (b) Same as above, but for a travel time of 21 ns.

(a) Mappa di 'arc length time' (vedi testo) calcolato con una finestra di 15 campioni (circa 2 ns) a 12 ns. Valori più alti della 'arc length' sono rappresentati in nero e sono proporzionali alla maggiore riflettività. (b) Come sopra, ma con tempi di percorrenza di 21 ns.

have similar waveform properties in both lateral and vertical dimensions, such as continuous layers of volcanic ash or other sediment. This type of attribute has been used to map potential petroleum reservoirs (GAO, 2007). For this study, we have applied 3D connectivity to the two reflective sequences discussed previously (Fig. 5) as well as to the entire volume. In order to demonstrate how this attribute works, we show connectivity anomalies from the lower reflectivity sequence (Fig. 5) in a perspective "workstation-style" view that visually integrates profiles and maps (Fig. 10). As can be seen from Figure 10, the map anomalies correlate with individual reflections and terminate at the edges of reflectors. We thus infer that the anomalies are generally responding to lateral stratigraphic coherency. The two anomalous areas of low semblance, amplitude, and coherency that we have been examining affect mainly the lower reflectivity sequence (Fig. 5). Computing connectivity within just this lower sequence indicates abrupt cessations in connectivity that define the edges of the square area on the NE part of the survey area and the roughly triangular area in the SW part of the survey as seen in perspective view (Fig. 10). The linearity of the connectivity terminations is easy to see in a flat map in which all connectivity anomalies from the lower sequence are displayed simultaneously (Fig. 11b). Showing, in identical format, only the anomalies from the upper reflectivity sequence (Fig. 11a) does not show any obvious linear

termination trends, which suggests that this sequence is less affected by the phenomenon (i.e., ground disruption) causing the changes in deeper reflections.

CONCLUSION

The landfill material and the presumed presence of previous archaeological excavations, which had been back-filled, combine to exacerbate the usual non-uniqueness of a geophysical interpretation of the subsurface. Although it was known that previous excavations and other disturbances of the ground had taken place, we did not know their exact locations. The results of 3D processing reveals distinct linear elements in map view that might be related to buried structures, back-filled excavations, or possibly to irregularities in the volcanic layering that fills and covers the site. We fortuitously were able to obtain an aerial photograph of the site that was apparently taken several years before our work commenced, but after previous workings (archaeological and otherwise) at the site. Figure 1 shows a rendering from this photograph, along with the boundary of the GPR survey area superimposed. One may clearly see a square area defined by vegetation and bare ground in the interior of the square; and a NW-SE-trending boundary defined by vegetation to the SW and bare ground to the NE (Fig. 1). A map presented by PAGANO (1992) indicates an excavation, which was made in the 1980s, in what appears to be about the same place as the square area on the photograph drawing and the square anomaly on the GPR map (time slice) images. We thus interpret the square area as being the site of a previous archaeological excavation (or possibly other disturbance of the ground), which was later back-filled and is represented on aerial photographs as a disturbed ground surface surrounded by low vegetation. The meaning of the line of vegetation cutting across the SW corner of the survey area is less clear, but appears to be the remains of an access road or filled trench. The effect of these two surface features, which were obliterated by the time of our 2007 survey, dominate the GPR data, especially in map (time slice) view.

The 3D visualizations thus reveal features that are related to previous, modern archaeological excavations or other disturbances of the ground. These features are expressed as strongly linear and/or rectilinear elements in the vertical views and time slices through the volume. The linear elements are expressed in vertical views as lateral disruptions of volcanic depositional layering, which is itself well expressed as sub-horizontal to wavy reflectivity. On the time slices, these lateral disruptions are evident as straight-line boundaries, which attest to their man-made origin. Other, less-well expressed linear elements may be related to archaeological features of interest, which would require confirmation by test-trenching.

The effect of previous disturbance or excavation of the ground is so well expressed on the GPR images due in part to the low attenuation of the volcanic sediment sequences and the sharp lateral truncations of these sequences. The volcanic layering is well charac-

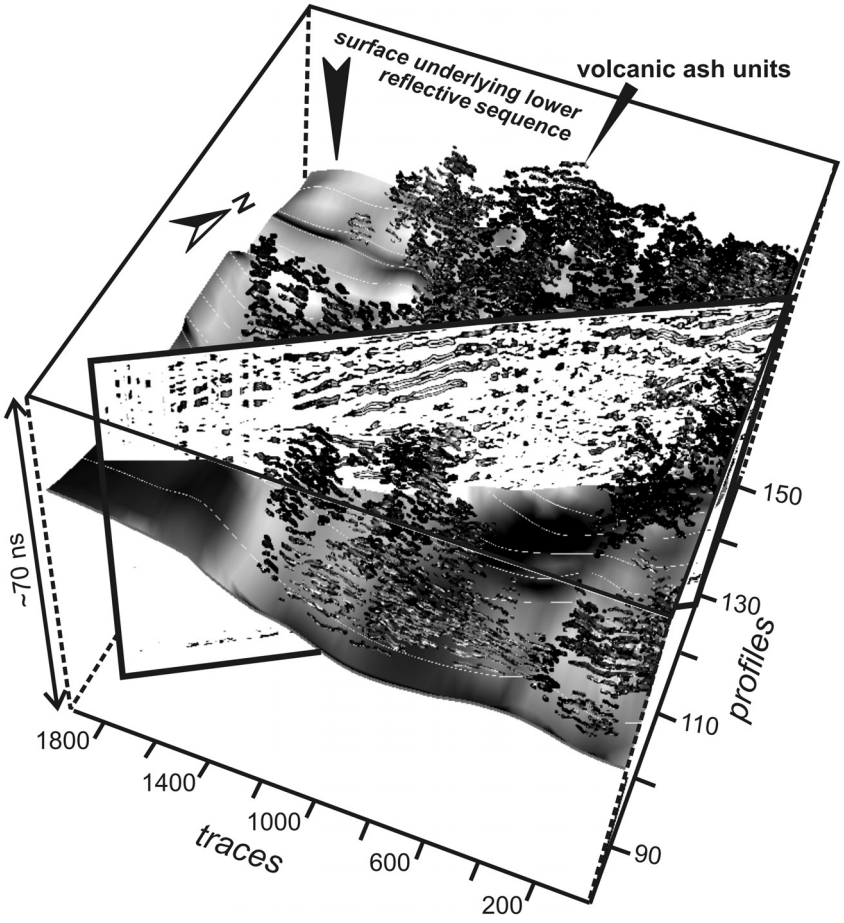

Figure 10 - Perspective ("workstation-style") view of connectivity anomalies from the deeper interval (interval 2 shown in Fig. 5a), interpreted as being mainly volcanic ash layers. The vertical view is extracted from the discontinuity volume (as shown in the vertical views depicted in the lower parts of Figures 5a, 5b, and 5c). The base of the second volcanic layer (Fig. 5) is shown as a gray-level surface. The connectivity anomalies are expressed as patterns above the surface and were computed with an imposed minimum size limit of 1000 voxels (i.e., the minimum number of voxels required to define the anomaly).

Visione prospettica delle anomalie di connettività dall'intervallo più profondo (l'intervallo 2 è mostrato in Fig. 5a), interpretate come dovute principalmente a livelli di cenere vulcanica. La sezione verticale è estratta dal volume di discontinuità (vedi testo) (come si mostra nelle viste verticali presenti nelle sezioni alla base delle figure 5a, 5b, 5c). La base del secondo livello vulcanico (Fig. 5) è mostrata come una superficie grigia. Le anomalie di connettività sono espresse come andamenti al di sopra della superficie ed sono calcolate con un limite di grandezza imposto di 1000 voxels.

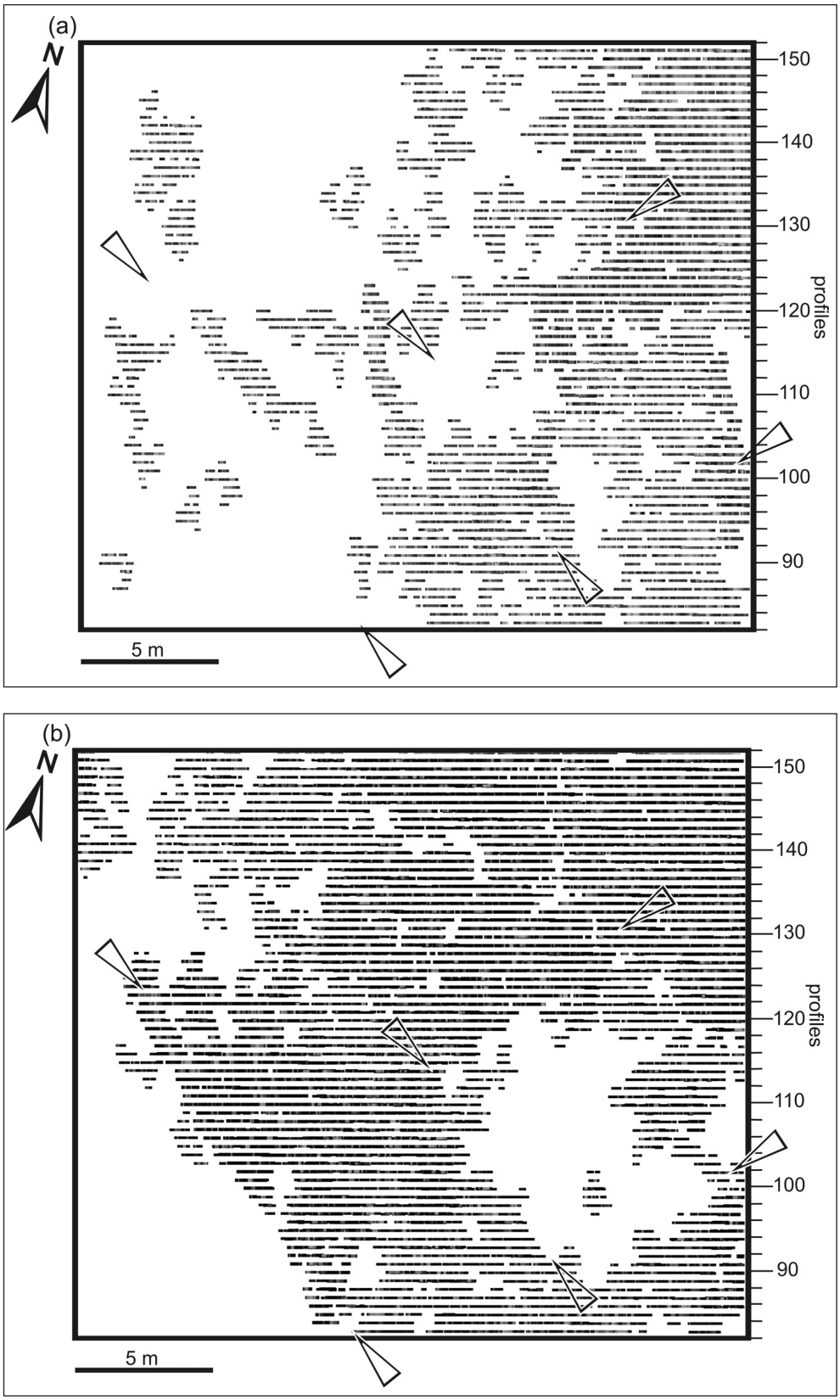

Figure 11 - (a) Volume-rendered time slice of connectivity anomalies corresponding to the upper reflectivity sequence (Fig. 5), 1-9 ns. (b) Same as above, but for lower reflectivity sequence (Fig. 5), 10-31 ns.

(a) Rappresentazione volumetrica delle anomalie di connettività corrispondenti alla sequenza di riflettività superiore (Fig. 5), 1-9 ns. (b) Come sopra, ma per la sequenza di riflettività inferiore (Fig. 5), 10-31 ns.

terized by the GPR data, as shown by the connectivity attribute. The discontinuity attribute responds well to imaging terminations within this layering. The arc length attribute responds particularly well to defining individual boundaries such as the SE edge of the square anomaly. The semblance attribute shows less precision than arc length. The volume rendering (18 ns to 24 ns) appears to show a high degree of precision, but this is partly an artifact of stacking anomalies from different depths onto on time slice view.

We demonstrate that GPR visualization can be effectively used for detecting subtle disturbances of volcanic soils. The precision of the visualization is improved with the application of processes designed for 3D seismic attribute processing, such as arc length, semblance, discontinuity, and connectivity attributes. From the several visualization examples presented herein, it should be clear that no single attribute will be appropriate for all targets. For example, the volume rendering (Fig. 7) reveals a feature as small as a pipe (Fig. 3) and the arc length can isolate it to 21 ns (Fig. 9); on the other hand, the semblance attribute (Fig. 8) is better for delineating bulk changes in reflectivity character, but may not be effective for small individual objects like a pipe. The visualization results will be used to guide future excavation at the site. The radar attribute images will provide constraints on interpreting the information revealed by future excavation and will also provide a shallow geological context

for understanding the physical character of the eruptive material that has covered the site episodically for the past two millennia.

ACKNOWLEDGMENTS

The authors gratefully acknowledge software grants from the Landmark (Halliburton) University Grant Program (GeoProbe™, SeisWorks3D™, and ProMAX2D™). Partial financial support for this project was provided by a Mentoring Environment Grant from Brigham Young University. The authors express their appreciation to the two journal reviewers for their useful and constructive comments.

REFERENCES

BAHORICH M., & FARME S. (1995) - *3-D seismic discontinuity for faults and stratigraphic features: The coherence cube*, The Leading Edge, v. **14**, p. 1053-1058.

CASTANIE L., BOSQUET F., & LEVY B. (2005) - *Advances in seismic interpretation using new volume visualization techniques*, First Break, v. **23**, p. 69-72.

CONYERS L. B. (2004) - *Ground-Penetrating Radar for Archaeology*, AltaMira Press, 203 pp.

CONYERS L. B. (2007) - *Ground-penetrating radar for archaeological mapping*, in WISEMAN J. & EL-BAZ F. (Editors), *Remote Sensing in Archaeology*, Springer, p. 329-344.

DE SIMONE A., SCARPATI C., MACFARLANE R. T., DE SIMONE G. F., KEITH J., PERROTTA A. , & MCBRIDE J. (2007) - *Eruptions and Settlements on Vesuvius' Northern Slope: the Apolline Project, International Congress People/environment relationships from the Mesolithic to the Middle Ages: recent Geo-Archaeological findings in Southern Italy*, Salerno, Italy, Sept. 4-7, 2007.

DE SIMONE G. F. (2007) - *Oltre la costa: il problema delle ville nell'entroterra vesuviano*, in CIARDIELLO R. (Editor), *La Villa Romana*, Orientale Editrice, p. 241-55.

GAO D. (2007) - *Application of three-dimensional seismic texture analysis with special reference to deep-marine facies discrimination and interpretation: Offshore Angola, west Africa*, AAPG Bulletin, v. **91**, p. 1665–1683.

GOODMAN D., SCHNEIDER K., PIRO S., NISHIMURA Y., & PANTEL A. G. (2007) - *Ground penetrating radar advances in subsurface imaging for archaeology*, in WISEMAN J. & EL-BAZ F. (Editors), *Remote Sensing in Archaeology*, Springer, p. 375-394.

MA C., & ROKNE J. (2004) - *3D Seismic Volume Visualization*, in ZHANG D. D., KAME, M., BACIU G., Editors, *Integrated Image and Graphics Technologies, The Springer International Series in Engineering and Computer Science*, Springer Netherlands, v. **762**, p. 241-262.

NEIDELL N. S., & TANER M. T. (1971) - *Semblance and other coherency measures for multichannel data*, Geophysics, v. **36**, p.482-497.

PAGANO M. (1992) - *Pollena Trocchia: scavo in località masseria De Carolis e ricognizioni nel territorio comunale*, Rivista di Studi Pompeiani **5** (1991/1992), p. 231-36.

PERROTTA A., SCARPATI C., LUONGO G., & AOYAGI M. (2006a) - *Burial of Emperor Augustus' villa at Somma Vesuviana (Italy) by post-79 AD Vesuvius eruptions and reworked (lahars and stream flow) deposits*. Journal of Volcanology and Geothermal Research, v.**158**, p. 445-466.

PERROTTA A., SCARPATI C., & LUONGO G. (2006b) - *Volcaniclastic resedimentation on the northern slope of Vesuvius as a direct response to eruptive activity*. Landslides, v. **3**, p 295-301

RUSSELL J. K., & STASIUK M. V. (1997) - *Characterization of volcanic deposits with ground-penetrating radar*, Bulletin of Volcanology, v. **58**, p. 515–527.

RUSSELL J. K., & STASIUK M. V. (2000) - *Ground-penetrating radar mapping of Minoan volcanic deposits and the late Bronze Age palaeotopography*, Thera, Greece, in McGUIRE W. J., GRIFFITHS D. R., HANCOCK P. L., & STEWART I. S., Editors, *Geological Society Special Publications*, v. **171**, p. 105-121.

RANA S., BURLEY S., & CHOWDHURY S. (2006) - *The application of hierarchical seismic attribute combination to high precision infill well planning in the South Tapti Field, offshore western India*, Geohorizons, January, p. 32-37.

RUST A. C., RUSSELL J. K., KNIGHT R. J. (1999) - *Dielectric constant as a predictor of porosity in dry volcanic rocks*, Journal of Volcanology and Geothermal Research, v. **91**, p. 79–96.

SANTACROCE R. (1987) - *Somma-Vesuvius*. C.N.R. Quad. Ric. Sc. **114/8**, p. 1-251.

SCHULTZ P.S., RONEN S., HATTORI M., CORBETT C. (1994) - *Seismic-guided estimation of log properties*, Part 1: A data-driven interpretation methodology, The Leading Edge, May, p. 305-311.

SHEETS P. D. (2005) - *The Ceren Site: A Prehistoric Village Buried by Volcanic Ash in Central America*, Wadsworth Publishing, 168 p.

SULPIZIO R., MELE D., DELLINO P. & LA VOLPE L. (2007) - *Deposits and physical properties of pyroclastic density currents during complex subplinian eruptions; the AD 475 (Pollena) eruption of Somma-Vesuvius, Italy*, Sedimentology, vol. **54**, p. 607-635.

ZHOU H-W. (1993) - *Traveltime tomography with a spatial-coherency filter*, Geophysics, v. **58**, p. 720-726.

Ms. ricevuto il 23 settembre 2008
Testo definitivo ricevuto l'8 aprile 2009

Ms. received: September 23, 2008
Final text received: April 8, 2009